Earth and Planetary Science Letters 599 (2022) 117865

Contents lists available at ScienceDirect

Earth and Planetary Science Letters

www.elsevier.com/locate/epsl

Liquidus determination of the Fe-S and (Fe, Ni)-S systems at 14 and 24 GPa: Implications for the Mercurian core

Allison Pease [a,b,*], Jie Li [b]

[a] Department of Earth and Environmental Sciences, Michigan State University, East Lansing, MI, 48824, USA
[b] Department of Earth and Environmental Sciences, University of Michigan, Ann Arbor, MI, 48109, USA

ARTICLE INFO

Article history:
Received 2 July 2022
Received in revised form 22 September 2022
Accepted 6 October 2022
Available online 18 October 2022
Editor: J. Badro

Keywords:
Mercury
Fe-S
(Fe, Ni)-S
liquidus
high pressure
core

ABSTRACT

Mercury has fascinated researchers for decades due to its sizable metallic core and weak magnetic field. The behavior of Fe-S and (Fe, Ni)-S systems provides constraints on core conditions and regimes of solidification to predict magnetic field strength. In this study, we investigate the melting behavior of the (Fe, Ni)-S system, a candidate composition to model the Mercurian core. We observe that the Fe-S liquidus has an inflection point at ~10 wt.% S at 14 GPa and ~11.5 wt.% S at 24 GPa, while (Fe, Ni)-S does not. At 24 GPa, Ni may lower the melting point of the Fe-S system by as much as 300 °C, indicating that solidification models and adiabatic calculations must account for the presence of Ni.

1. Introduction

The composition and structure of Mercury have been studied for decades. Ground observations revealed that Mercury has an average density of 5.427 g cm^{-3}, which led to the inference that it possessed a large metallic core that makes up 68-85% of the planet's radius (Anderson et al., 1996; Riner et al., 2008). Mariner 10 was launched in 1973; upon passing Mercury, it detected a weak magnetic field. Radio-based observations of the amplitude of the planet's longitudinal librations indicated that the core was partially molten (Margot et al., 2007). In 2008, MESSENGER approached Mercury and determined the surface geochemistry using x-ray, gamma-ray, and neutron spectrometers (Nittler et al., 2018). MESSENGER detected a FeO-poor surface and a high S/Si ratio (0.05-0.15), indicating the planet is reduced and rich in S (Zurbuchen et al., 2008; Nittler et al., 2018).

MESSENGER provided evidence of surface geochemistry, but the chemistry and light element abundance of the Mercurian core is debated. The core composition is directly linked to the state, pressure, temperature, structure, and bulk composition of the planet. The pressure and temperature range of the Mercurian core are estimated to be 7-40 GPa and 1400-2000 °C, respectively (Harder and Schubert, 2001; Chen et al., 2008; Michel et al., 2013; Tosi et al., 2013; Knibbe and van Westrenen, 2018; Pommier et al., 2019). The lack of seismic evidence on Mercury introduces uncertainty regarding the current state and structure of the Mercurian core. Stevenson et al. (1983) concluded that a core composed of pure Fe or Fe-Ni would be solid at the temperature-pressure conditions of the Mercurian core; therefore, the observation of a partially or fully molten core indicates the presence of light elements (S, Si, O, C, H), lowering the melting point of Fe.

The abundance of S on the surface of Mercury led to the inference that the interior was reduced (IW-3 to IW-7) (McCubbin et al., 2012; Zolotov et al., 2013; Nittler et al., 2018) and that S and Si are abundant in the Mercurian core (Nittler et al., 2018). Silicon was selected because of its tendency to alloy with Fe under reducing conditions (Gessmann et al., 2001; Malavergne et al., 2004) and the partition coefficient of Si being correlated to S content (Tao and Fei, 2021). The composition of light elements in the Mercurian core is not precisely constrained, but the core is predicted to be a Fe-Ni alloy with 0-20 wt.% Si and 0-17 wt.% S; recent studies predict there is more Si in the core relative to S (16 and 7 wt.%, respectively) (Malavergne et al., 2010; Hauck II et al., 2013; Namur et al., 2016; Nittler et al., 2018; Pommier et al., 2019).

* Corresponding author at: 288 Farm Ln bldg rm 207, East Lansing, MI 48824, United States of America.
E-mail addresses: peaseall@msu.edu (A. Pease), jackieli@umich.edu (J. Li).

https://doi.org/10.1016/j.epsl.2022.117865
0012-821X/

Melting experiments have been conducted on the Fe-alloy system to determine mechanisms of core solidification and provide insight into the weak magnetic field observed by MESSENGER. Terrestrial bodies, such as Earth, produce magnetic fields through the convection of a liquid Fe-alloy. The intensity of Mercury's magnetic field is a fraction of the Earth's magnetic field (Ness et al., 1976), which implies a different core state. Possible regimes of solidification include the formation of solid or liquid Fe, Fe_3S, Fe-S, or FeSi at the core-mantle boundary, interior, or center of the core. The styles of solidification lead to unique structures for the Mercurian core: Fe snow in one or more locations (Chen et al., 2008), the formation of a Fe sulfide core (Stewart et al., 2007), or a Fe-S liquid to FeS solid shell surrounding a Si-rich inner core (Malavergne et al., 2010, 2014; Manthilake et al., 2019). The formation of a Fe-S layer surrounding a Si-bearing inner layer was proposed because Si is not miscible in Fe-S at low pressures (Malavergne et al., 2004). Iron snow and a Fe-S shell may produce a weakened magnetic field by shielding or canceling fields with opposite polarities (Vilim et al., 2010).

The state of the Fe-S shell is linked to the thermal profile of the Mercurian core and the melting behavior of Fe-alloys. The Fe-S shell is located at the core-mantle boundary and is devoid of Si (Malavergne et al., 2004). Previous studies have predicted a temperature difference of 600 °C throughout the core; this temperature gradient has been explained using adiabatic and sub-adiabatic heat flow that results in the formation of a solid, liquid, or not existent Fe-S shell at the core-mantle boundary (Chen et al., 2008; Dumberry and Rivoldini, 2015; Knibbe and van Westrenen, 2018; Pommier et al., 2019; Manthilake et al., 2019). Dumberry and Rivoldini proposed sub-adiabatic heat flow in 2015 to generate a thermally stratified core based on the adiabatic temperature gradient being larger than the heat flow predicted from conductivity measurement on FCC-Fe (Deng et al., 2013).

The core's thermal profile depends on the conductivity of the Fe-alloy at the core-mantle boundary because the Mercurian mantle has been predicted to absorb a few mW/m^2. The observed Fe conductivity of 125 W/(mK) results in a 45-100 mW/m^2, leading to sub-adiabatic heat flow (Dumberry and Rivoldini, 2015). However, the FeS conductivity is thought to be 4 W/(mK), significantly lower than pure Fe (Manthilake et al., 2019). Meanwhile, (Fe, Ni)-S alloys were found to range from 12-20 W/(mK) at 4.5-8 GPa, resulting in an (adiabatic) heat flow of a few mW/m^2 on small terrestrial bodies (Pommier, 2020). The conductivity of Fe alloys will significantly impact the temperature of the Mercurian core; however, given low conductivity values reported for (Fe, Ni)-S, the Mercurian core may behave adiabatically, similar to the adiabat proposed by Chen et al. (2008).

Additional information on the melting behavior of Fe-alloy systems is needed to constrain the state of the Mercurian core. For example, the concavity of the Fe-S and (Fe, Ni)-S liquidus curves is not well constrained at pressures >14 GPa. Studies on the Fe-S system, conducted at <20 GPa, have observed an inflection point between 8-14 wt.% S (Chen et al., 2008; Buono and Walker, 2011; Pommier et al., 2018). Whether such an inflection point persists at higher pressures is unknown because previous studies focused on constraining the eutectic melting point (Fei et al., 2000; Li and Agee, 2001; Stewart et al., 2007). Previous studies, (Stewart et al., 2007; Chen et al., 2008; Pommier et al., 2018), have also focused on the Fe-S system and omitted Ni, a major element in the core, because it proposed that Ni did not affect the melting point of Fe (Stewart et al., 2007). Recently, that observation has been challenged by studies demonstrating that Ni can change the melting point of Fe (Zhang et al., 2016; Boccato et al., 2017; Gilfoy and Li, 2020; Liu and Li, 2020).

In this study, we conduct multi-anvil experiments on the Fe-S system at 14 and 24 GPa to examine if the liquidus shape observed by Chen et al. (2008) persists to higher pressures and if Ni lowers the melting point of the Fe-S system at 24 GPa.

2. Experimental methods

Melting experiments were conducted using the Walker-type multi-anvil apparatus at the University of Michigan. The starting materials were mixtures of Fe (Alfa Aesar, 99.998% purity, CAS#7439-89-6, 10621), Ni (Alfa Aesar, 99.999% purity, CAS#7440-02-0, 12966), and FeS (Alfa Aesar, 99.98% purity, CAS#1317-37-9, 22388). Compositions ranging from $Fe_{99\text{-}75}S_{1\text{-}25}$, $Fe_{95\text{-}87}Ni_4S_{1\text{-}9}$, and $Fe_{87\text{-}79}Ni_{12}S_{1\text{-}9}$ (wt.%) were mixed in an agate mortar and dried in a vacuum oven for at least 24 hours before loading. A compositional range was selected to optimize the melt fraction and minimize the number of fully molten experiments.

Modified COMPRES 10/5 or 8/3 assemblies (Leinenweber et al., 2012) were used for 14 GPa and 24 GPa experiments (Fig. 1). The pressure was calibrated using $MgSiO_3$ and Mg_2SiO_4 phase transitions (Gilfoy and Li, 2020). Previous studies demonstrate that temperature can impact the pressure of the sample. Leinenweber et al. (2012) observed a pressure drop of 2 GPa after heating the sample from 800 °C to 1800 °C. However, Fei et al. (2004) observed the pressure increase by 2 GPa when they sintered the sample (680 ton), then heated the sample from 1226 °C to 2026 °C (1400 ton) (Fei et al., 2004). These experiments report a pressure drift at high temperatures relative to low temperatures from *in situ* XRD experiments. The *in situ* experiments insert an X-ray transparent window; this slightly modifies the experimental setup from the *ex-situ* setup used in this study. Given Fei et al.'s (2004) results, sintering the sample may offset the pressure drift. In this study, we sinter the sample (details below) and estimate a pressure uncertainty of ±2 GPa.

We conduct 24 GPa experiments with one or two samples in each experiment. Dual-chamber experiments allowed for a simultaneous Fe-S and (Fe, Ni)-S experiment at the same pressure-temperature conditions. Single-chamber experiments at 24 GPa and some single-chamber experiments at 14 GPa included a thermocouple, and the sample was placed at the center of the cell (Fig. 1). The double-chamber experiments at 24 GPa and some single-chamber experiments at 14 GPa did not include a thermocouple, and the temperature is inferred based on a calibrated power curve (shown in the supplementary material). Previous studies observed that using a power curve can reproduce the temperature-power relation within 5% (Gilfoy and Li, 2020), making the temperature uncertainty comparable to the thermal gradient observed in experiments with a thermocouple (Leinenweber et al., 2012).

Once loaded into the press, the sample was brought to the target pressure of 14 GPa in 6-8 hours and 24 GPa in 8-12 hours. Fourteen GPa was chosen to directly compare experiments to Chen et al. (2008). While 24 GPa was selected because it is the highest stable pressure achievable in the University of Michigan multi-anvil apparatus and directly compares liquidi with different Ni concentrations at 23 GPa (Stewart et al., 2007).

At 5 GPa, the sample was sintered at 600-700 °C to lower the porosity of the MgO capsule, prevent contamination between the sample and the Re-heater, and minimize potential pressure drift. When the target pressure was reached, the sample was heated at 100 °C per minute to the target temperature of 1200-1900 °C. All samples were held at target temperatures for 3 to 30 minutes and then rapidly quenched to room temperature. Equilibrium was confirmed based on similar S abundances in the solid phase and the observation of a smooth boundary between the melt and solid phase (Gilfoy and Li, 2020) (Fig. 2). The recovered sample was exposed using 180, and 600 grit silicon carbide paper and polished using 0.3-micron Al_2O_3 powder.

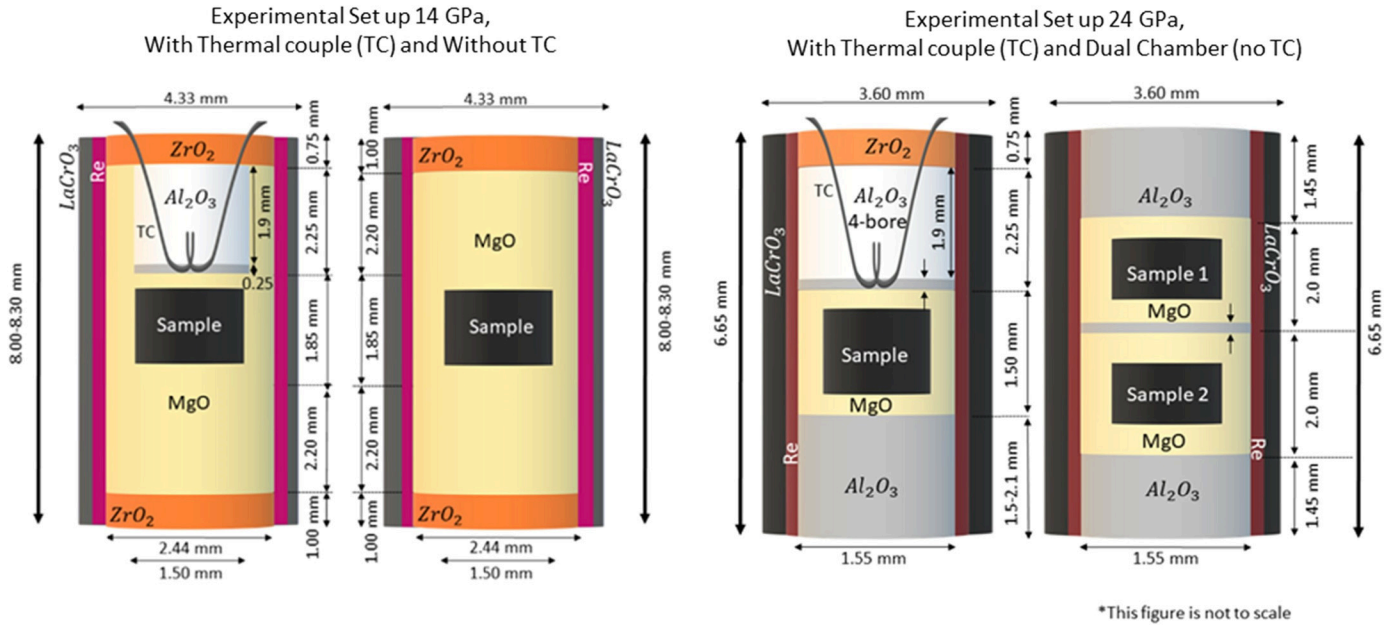

Fig. 1. Configurations of 14 GPa and 24 GPa experiments. The 14 GPa experiments were conducted using the original COMPRES 10/5 assembly, and two experiments were conducted without a thermocouple present. The 24 GPa experiments were conducted using a modified COMPRES 8/3 assembly with a shorter Al_2O_3 plug or a dual-chamber configuration.

Table 1
Experimental conditions and results on Fe-S system at 14 GPa.

Experiment Name	Temp. (°C)	Time (min)	Phase	Wt.% S	Wt.% Fe	Wt.% Total	# of Points
M020419	1750 (50)	15	Solid	N/A	N/A	N/A	
			Liquid focused	1.5 (3)	99.4 (3)	101.1 (6)	99
			Liquid defocused	1.8 (6)	99.1 (6)	100.9 (8)	25
M021217	1500 (100)	15	Solid	0.18 (1)	100.6(2)	100.8 (3)	9
			Liquid focused	7.2 (7)	93.0 (7)	100.2 (9)	98
			Liquid defocused	8.4 (8)	91.8 (8)	100 (1)	25
M021019	1400 (50)	15	Solid	0.16 (1)	101.0 (3)	101.2 (3)	6
			Liquid focused	6.6 (7)	93.7 (8)	100 (1)	100
			Liquid defocused	6.8 (5)	93.7 (5)	100.5 (7)	25
M113016	1350 (100)	15	Solid	0.22 (3)	99.8 (3)	100 (4)	9
			Liquid focused	12.2 (5)	87.9 (5)	100.2 (7)	199
			Liquid defocused	11.9 (4)	88.4 (4)	100.3 (6)	25
M092819	1000 (50)	30	Solid	36 (1)	64 (1)	100 (1)	1*
			Liquid defocused	23.9 (3)	75.7 (3)	99.6 (4)	140

Notes: The composition was determined in an EPMA using both focused and defocused grids. The beam we calibrated to a point in the focused grid and broadened in the defocused grid. Both agree within uncertainties. The uncertainties in liquid compositions are standard errors of the means, and those in solid compositions are standard deviations. The notation can be read as 75.7 (3) is equal to 75.7 ± 0.3. Temperature uncertainty is estimated to be 50 °C when a thermocouple is used and 100 °C when a power curve is used.
*Experiment M092819 (solid) has one composition value; the composition is based on SEM/EDS measurements.
N/A indicates that the sample is fully molten and there is no coexisting solid phase.

Samples were carbon-coated and analyzed using a JEOL-Scanning Electron Microscope (SEM) and CAMECA SX-100 Electron Probe Micro-analyzer (EPMA) at the University of Michigan. Chalcopyrite was used as a dual standard for Fe (LIF) and S (LPET). Nickel metal was used as the Ni standard (LLIF). An accelerating potential of 20 kV and a 15 nA beam current were used with peak counting times of 10 seconds.

The compositions of the 14 GPa samples were measured using a focused beam with a four-micron step covering a 100-point EPMA grid and a 10-micron beam with a 10-micron step covering a 25-point EPMA grid. The compositions of the 24 GPa samples were also analyzed using a combination of a focused (<1 μm) and a defocused (10 μm) beam. The two-beam settings were compared to check validity.

3. Results and discussion

3.1. Experimental data

Five experiments at 14 GPa yielded partially or fully molten products at 1000-1750 °C (Table 1). One experiment was on the sulfur-rich side of the eutectic. The compositions from focused and defocused-beam analyses agree within uncertainties.

Nineteen experiments at 24 GPa yielded results between 1200 and 1900 °C (Table 2, Table 3). For the single-chamber experiments, seven were on the Fe-S system, and eight were on the (Fe, Ni)-S system. The (Fe, Ni)-S products contained 11-14 wt.% Ni. Four dual-chamber experiments produced Fe-S in one chamber and (Fe, Ni)-S with 4-5 wt.% Ni in the other.

Table 2
Experimental conditions and results on Fe-S system at 24 GPa.

Experiment Name	Phase	Temp. (°C)	Time (min)	wt.% S	wt.% Fe	wt.% Ni	wt.% Total	# of Points
M062718	Solid	1900 (100)	10	0.22 (4)	99.9 (4)	N/A	100.1(4)	32
	Melt			3.4 (3)	97.0 (4)	N/A	100.4 (5)	182
M061118	Solid	1800 (150)	3	N/A	N/A	N/A	N/A	
	Melt			5.0 (4)	94.8 (4)	N/A	99.8 (5)	211
M083018*	Solid	1700 (50)	10	0.37 (4)	100.5 (3)	N/A	100.9 (3)	8
	Melt			6.7 (5)	94.0 (5)	N/A	100.7 (7)	95
M061318	Solid	1650 (100)	3	N/A	N/A	N/A	N/A	
	Melt			7.0 (4)	92.7 (4)	N/A	99.7 (6)	208
M071318*	Solid	1600 (100)	10	N/A	N/A	N/A	N/A	
	Melt			8.3 (5)	91.6 (5)	N/A	99.9 (7)	97
M060818	Solid	1500 (100)	3	0.7 (6)	98.7 (6)	N/A	99.4 (8)	17
	Melt			8.6 (6)	90.4 (6)	N/A	99.0 (8)	113
M062018	Solid	1550 (50)	5	0.4 (2)	100.0 (4)	N/A	100.4 (3)	46
	Melt			10.0 (3)	90.1 (3)	N/A	100.1 (1)	72
M082818*	Solid	1500 (50)	20	0.16 (4)	100.8 (3)	N/A	100.9 (3)	7
	Melt			12.6 (4)	86.9 (3)	N/A	99.5 (5)	153
M062518	Solid	1300 (50)	10	0.56 (9)	100.0 (6)	N/A	100.6 (6)	21
	Melt			14.6 (3)	85.3(5)	N/A	99.9 (6)	22
M061818	Solid	1200 (100)	3	0.69 (5)	98.5 (3)	N/A	99.2 (3)	44
	Melt			14.0 (2)	85.3 (2)	N/A	99.3 (3)	242
M082118*	Solid	1200	30	0.88 (4)	99.4 (6)	N/A	100.3 (6)	3
	Melt			14.2 (5)	87.1 (2)	N/A	100.8 (6)	24

Notes: The compositions were determined using both focused and defocused grids. The numbers in parentheses are uncertainties. Compositional uncertainties are standard deviations for solids and standard errors of the means for liquids. Temperature uncertainties are estimated based on the distance of the thermocouple and sample chamber from the center of the cell and range from 50 to 150 °C.
* indicates a dual-chamber sample.
N/A indicates that the sample is fully molten, and there is no coexisting solid phase.

Table 3
Experimental conditions and results on (Fe, Ni)-S system at 24 GPa.

Experiment Name	Phase	Temp. (°C)	Time (min)	wt.% S	wt.% Fe	wt.% Ni	wt.% Total	# of Points
M111518	Solid	1900 (100)	15	0.09 (2)	87.4 (5)	13.3 (3)	100.8 (6)	9
	Melt			1.6 (5)	85.2 (8)	13.3 (2)	100 (1)	49
M111618	Solid	1750 (50)	10	0.15 (2)	86.6 (4)	13.91 (7)	100.7 (4)	4
	Melt			3.9 (6)	82.5 (6)	13.79 (1)	100.2 (8)	30
M083018*	Solid	1700 (50)	10	0.34 (4)	95.5 (3)	4.97 (1)	100.8 (3)	3
	Melt			3.8 (5)	91.6 (5)	4.74 (3)	100.1 (7)	71
M102818	Solid	1700 (100)	10	N/A	N/A	N/A	N/A	
	Melt			6.4 (2)	81.5 (2)	12.19 (4)	100.7 (3)	27
M111418	Solid	1600 (50)	15	N/A	N/A	N/A	N/A	
	Melt			5.5 (3)	82.4 (3)	12.12 (3)	100.0 (4)	38
M071318*	Solid	1600 (100)	10	0.24 (1)	95.8 (2)	4.7 (2)	100.7 (3)	5
	Melt			5.1 (2)	91.8 (2)	3.90(2)	100.8 (3)	35
M102618	Solid	1500 (100)	10	0.48 (3)	87.9 (7)	11.88 (8)	100.3 (7)	10
	Melt			8.0 (3)	81.3 (3)	11.29 (3)	100.5 (4)	26
M082818*	Solid	1500 (50)	20	0.3 (1)	95.2 (6)	4.96 (6)	100.5 (6)	15
	Melt			6.1 (7)	88.8 (7)	4.55 (5)	99 (1)	46
M110718	Solid	1400 (50)	10	0.19 (1)	87.5 (5)	12.7 (1)	100.4 (5)	10
	Melt			9.8 (2)	77.2 (3)	12.80 (3)	99.8 (3)	26
M102518	Solid	1300 (50)	10	0.56 (8)	89.2 (8)	11.0 (4)	100.8 (9)	4
	Melt			12.4 (7)	77.3 (9)	10.7 (1)	100 (1)	19
M110818	Solid	1200 (50)	20	0.3 (1)	89.6 (5)	10.9 (2)	100.8 (5)	9
	Melt			13.1 (2)	75.9 (3)	11.17 (3)	100.2 (4)	22
M082118*	Solid	1200 (50)	30	0.64 (3)	95.8 (7)	4.5 (6)	100.9 (9)	9
	Melt			13. 5 (2)	81.6 (2)	4.85 (7)	100.1 (3)	11

Notes: The compositions were determined using both focused and defocused grids. The numbers in parentheses are uncertainties. Compositional uncertainties are standard deviations for solids and standard errors of the means for liquids. Temperature uncertainties are estimated based on the distance of the thermocouple and sample chamber from the center of the cell and range from 50 to 150 °C.
* indicates a dual-chamber sample.
N/A indicates that the sample is fully molten, and there is no coexisting solid phase.

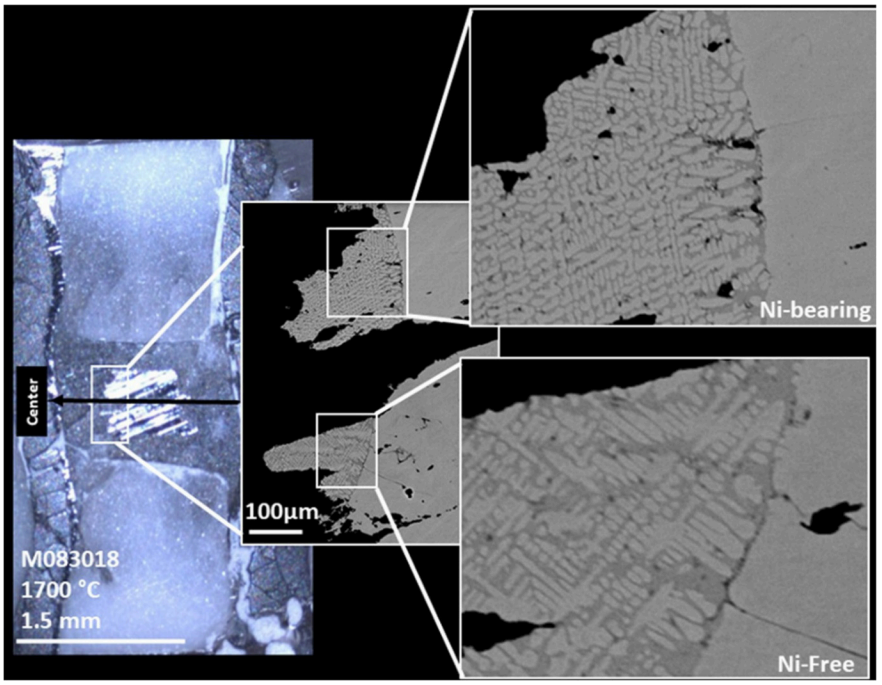

Fig. 2. Configuration and product from dual-chamber experiment M083018. The optical image of the roughly polished experimental product is on the left, showing the two sample chambers in the cylindrical heater. The samples are about 50 μm apart and separated by MgO, denoted with an artificial black line representing the center of the heater. The center image and right images are BSE images of (Fe, Ni)-S (upper) and Fe-S (lower).

3.2. Textural variation

The recovered Fe-S and (Fe, Ni)-S liquids exhibit dendritic textures containing bright iron-rich dendrites and dark sulfur-rich matrix (Fig. 2). In S-poor liquids, Fe dendrites are dominant, and a dark matrix exists as an interstitial phase. In S-rich liquids, Fe dendrites are scattered in the matrix, sometimes with a non-uniform distribution. The texture can be used to estimate the S content of the liquid.

The Ni-free and Ni-bearing experiments showed similar trends in textural variation with temperature. When the S concentration is lower, the dendrites are abundant, larger, and homogeneous; lower S concentrations occur at higher temperatures. In the dual-chamber experiments, it is apparent that the Ni-bearing liquid has fewer Fe dendrites than the Ni-free liquid at the same pressure and temperature conditions. The Dual-chamber experiment M083018 highlights this relationship in Fig. 2. This relationship implies that the Ni-bearing liquidus occurs at a lower temperature than the Ni-free liquidus (Fig. 4).

3.3. Liquidus curve at 14 GPa

Five experiments yielded constraints on the Fe-S liquidus curve at 14 GPa (Table 1, Fig. 3). Together with experimental results from Chen et al. (2008), Anzellini et al. (2013), and Boehler (1992), the 14 GPa liquidus on the iron-rich side of the eutectic was fitted using a fourth-order polynomial. The results in this study confirm that an inflection point exists on the iron-rich side of the eutectic at ∼10 wt.% S. Experiment M092819 provides the first constraint on the liquidus curve on the sulfur-rich side of the eutectic, suggesting that it is lower than the liquidus proposed by Fei et al. (1997).

3.4. Liquidus curves at 24 GPa

3.4.1. From single chamber experiments

Nineteen experiments at 24 GPa yielded constraints on the Fe-S and (Fe, Ni)-S liquidus curves (Tables 2 and 3). Seven single-chamber experiments on the Fe-S system, five partially molten and two fully molten, suggest the presence of an inflection point at ∼11.5 wt.% S (Fig. 4a). Eight single-chamber experiments on the (Fe, Ni)-S system, six partially molten and two fully molten, suggest the (Fe, Ni)-S liquidus curve for 11-14 wt.% Ni is located at lower temperatures than the Fe-S liquidus and does not contain an inflection point. The curve is slightly concaved upwards. The location and shape are consistent with the results of Gilfoy and Li (2020) at 20 GPa.

3.4.2. From dual-chamber experiments

The four dual-chamber experiments at 24 GPa directly compare the Ni-free and Ni-bearing Fe-S liquidus curves. In this set of experiments, the Ni concentration ranged from 4-5 wt.%. The (Fe, Ni)-S liquidus is at lower temperatures than the Fe-S liquidus (Fig. 4b). The inflection point of the Fe-S system and its absence in the (Fe, Ni)-S system are confirmed.

3.5. Comparison to published data

3.5.1. Eutectic point and Fe-Ni melting point

The Fe-S eutectic point has been determined at a range of pressures. As the pressure increases, the eutectic shifts to a lower S concentration. The eutectic temperature decreases with pressure between 1 bar and 14 GPa and increases at higher pressures. The eutectic composition at 24 GPa is interpolated between those at 23 GPa (Stewart et al., 2007) and 25 GPa (Li and Agee, 2001). The melting point of Fe at 24 GPa is calculated from the curve proposed by Anzellini et al. (2013), and it is ∼150 °C higher than the melting point of Fe shown in Stewart et al. (2007).

The (Fe, Ni)-S eutectic has been partially constrained at a range of pressures. Stewart et al. (2007) determined the eutectic points of the (Fe, Ni)-S system containing 36 wt.% Ni at 23 and 40 GPa. They did not examine how the concentration of Ni affected the (Fe, Ni)-S eutectic composition and temperature. Zhang and Fei (2008) observed that the temperature of the eutectic point decreases with increasing Ni content. We estimated the eutectic points of (Fe, Ni)-

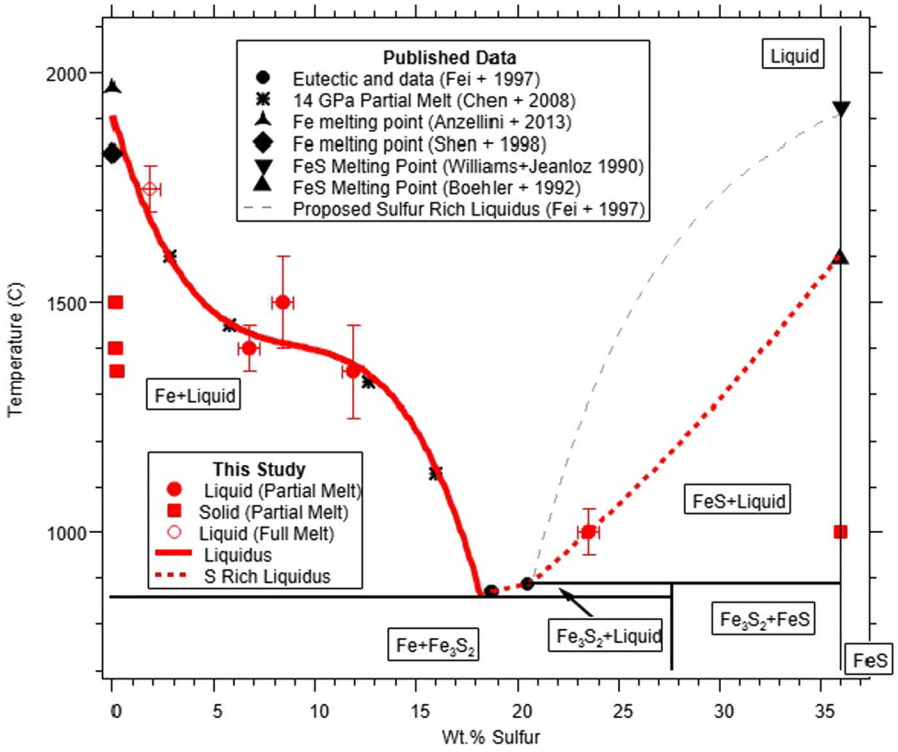

Fig. 3. Fe-S liquidus at 14 GPa. The liquidus curve for the iron-rich side of the eutectic (solid red curve) is based on experimental data from this study (the red solid squares and circles represent coexisting solids and melts, respectively, while the open circles represent stand-alone melts) and published data (stars from Chen et al. (2008)), the solid circles for the eutectic and peritectic points from Fei et al. (1997). The melting point of Fe is from Shen et al. (1998) and Anzellini et al. (2013). The dashed liquidus curve on the sulfur-rich side of the eutectic is drawn through the data point from this study and the melting point of FeS (Williams and Jeanloz, 1990; Boehler, 1992; Fei et al., 1997). (For interpretation of the colors in the figure(s), the reader is referred to the web version of this article.)

S systems at 24 GPa containing 4-5 wt.% Ni to be 16.8 wt.% S and 1020 °C; 11-14 wt.% Ni to be 17 wt.% S and 980 °C, shown in Fig. 4 (Stewart et al., 2007; Zhang and Fei, 2008).

A recent study suggests that the melting point of Fe-Ni is higher than that of pure Fe by 2 °C/wt.% Ni (Boccato et al., 2017). Accordingly, we estimated the melting point of Fe-Ni with 11-14 wt.% Ni and 4-5 wt.% Ni to be 2224 °C and 2210 °C, respectively.

3.5.2. Fe-S liquidus at 1 bar to 40 GPa

At 1 bar, the Fe-S liquidus has an inflection point, which vanishes at elevated pressures (Buono and Walker, 2011), and then reappears at 14 GPa (Chen et al., 2008) and persists at 20 GPa (Pommier et al., 2018). Results on Fe-S experiments at 24 GPa confirm the presence of an inflection point in the liquidus curve, contrary to the concave-downward curves proposed by Stewart et al. (2007). We note that the data points of Stewart et al. (2007) are consistent with the fitted liquidus curve in this study, shown in Fig. 4.

3.5.3. (Fe, Ni)-S liquidus curves at 5 GPa to 40 GPa

Four previous studies determined the liquidus curves of the (Fe, Ni)-S system at 5, 20, 23, and 40 GPa. Experiments at 5 and 20 GPa indicated that Ni lowers the Fe-S liquidus (Gilfoy and Li, 2020; Liu and Li, 2020), whereas those at 23 and 40 GPa observed little to no change when Ni was added to the Fe-S liquidus (Stewart et al., 2007). In this study, we observe that the (Fe, Ni)-S liquidus (11-14 wt.% Ni and 4-5 wt.% Ni) occurs at lower temperatures than the Ni-free system at 24 GPa. The discrepancy between this study and Stewart et al. (2007), which focused on determining the eutectic melting points of the Fe-S and (Fe, Ni)-S system, may result from different experimental goals.

The effect of Ni is not well understood. Based on this study and Stewart et al. (2007), it appears that 4-5 wt.% Ni lowers the melting point of the Fe-S system more than 11-14 wt.% Ni, which, in turn, reduces the melting point of the Fe-S system more than 36 wt.% Ni (Fig. 4). In other words, adding a small amount of Ni has a large effect in depressing the melting point, but increasing the amount of Ni shifts the liquidus curve towards the Ni-free system. To date, the (Fe, Ni)-S liquidus and eutectic have been investigated in systems with different concentrations of Ni, and therefore the results are not directly comparable (Stewart et al., 2007; Zhang and Fei, 2008; Morard et al., 2011; Gilfoy and Li, 2020; Liu and Li, 2020). A range of Ni concentrations needs to be explored to constrain how different concentrations of Ni impact the Fe-S liquidus.

4. Implications for Mercury's core

4.1. Nickel lowers the melting point

In this study, we observe that at 24 GPa, Ni depresses the Fe-S melting point by as much as 300 °C (Figs. 4 and 5). Qualitatively this is consistent with previous studies at <7 GPa (Liu and Li, 2020) and an indirect comparison between two studies at 20 GPa (Pommier et al., 2018; Gilfoy and Li, 2020). The effect of Ni varies with pressure. At 5 GPa, Ni depresses the Fe-S liquidus the most at low S concentrations and the least at 10 wt.% S. The opposite is true at 20 GPa. At 24 GPa, the maximum effect occurs at, ~11-13 wt.% S, the inflection point (Fig. 5).

For predicted compositions of the Mercurian core, which contains 0-17 wt.% S, Ni changes the melting point of Fe-S by 2 °C/wt.% Ni at 0 wt.% S (Boccato et al., 2017), and up to ~-300 °C for 1-16 wt.%S (Fig. 6). Fig. 6 compares the pressure-temperature liquidi for the Fe-S and (Fe, Ni)-S system from 5 to 24 GPa. Ni-Free (Fe-S) liquidi are fifth-order polynomial fits to published data (Fei et al., 2000; Stewart et al., 2007; Chen et al., 2008; Buono and Walker, 2011; Pommier et al., 2018) and this study. Ni-Bearing

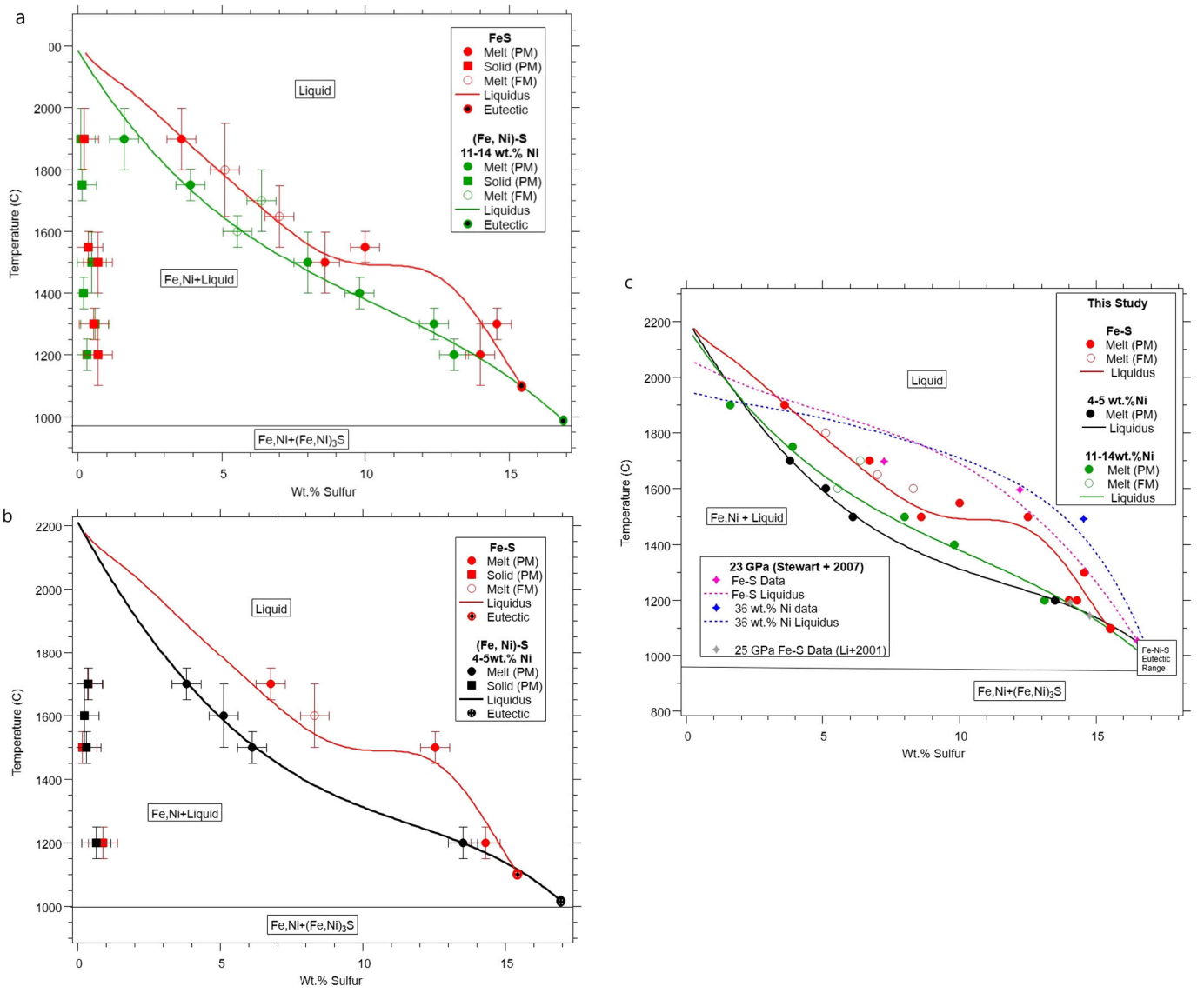

Fig. 4. Fe-S and (Fe, Ni)-S liquidus curves at 23-25 GPa. The Fe-S liquidus is shown in red; the (Fe, Ni)-S liquidus is shown in black for 4.5 wt.% Ni and in green for 12.5 wt.% Ni. The solid squares and circles represent the coexisting solid and liquid phase (PM-partial melt), respectively, while the open circles represent stand-alone melts (FM-fully molten). The eutectic point is a multi colored circle and is approximated based on Li and Agee (2001), Stewart et al. (2007), and Zhang and Fei (2008). The melting point of Fe is calculated according to the fitted curve in Anzellini et al. (2013) and Boccato et al. (2017); note these values are different than the melting point of Fe reported in Stewart et al. (2007). 4a, are liquidus curves from single chamber experiments at 24 GPa. 4b, are liquidus curves from dual-chamber experiments. 4c compares this study and the literature data around 24 GPa. The dashed pink and blue lines are liquidus curves proposed by Stewart et al. (2007) for the Fe-S and (Fe, Ni)-S (36 wt.% Ni), respectively. The pink and blue stars are the experimental data from Stewart et al. (2007) for the Fe-S and (Fe, Ni)-S (36 wt.% Ni), respectively. The grey stars are experimental data from Li and Agee (2001) at 25 GPa.

((Fe, Ni)-S) liquidi are linear fits between published data (Gilfoy and Li, 2020; Liu and Li, 2020) and this study. Stewart et al. (2007) are omitted from the fit in the Fe-S system at 23 GPa and are not included for the (Fe, Ni)-S system at 23 or 40 GPa due to the small sample size.

We observe that a small amount of Ni (5-12%) lowers the melting point more than 36 wt% Ni. To confirm this trend, we have collected a few data points at 20% and 50% Ni; however, due to the sparse data collected, we have only included these values in the supplementary material. From this study, we observe a linear trend between melting temperature and increase in Ni content. The variation in behavior occurs at the inflection point in the Fe-S system when 0 wt.% Ni is present.

The presence of an inflection point in the Fe-S liquidus curve at 24 GPa reflects repulsive interaction between Fe and Fe-S species in the liquid, which leads to reduced stability of a single liquid with respect to the solid-liquid coexistence (Saunders et al., 1998). In the Fe-S binary system, an inflection point exists at 1 bar, becomes less prominent with increasing pressure, and is nearly absent at 6-10 GPa (e.g., Liu and Li, 2020). At higher pressures, however, an inflection point appears again at 14 GPa (Chen et al., 2008), 20 GPa (Pommier et al., 2018), and 24 GPa (this study). The reappearance of the inflection point seems to correlate with the stabilization of Fe_3S_2 and Fe_3S eutectic points between Fe and the intermediate Fe-S compounds near 14 GPa and 21 GPa, respectively, indicating concurrent bonding change in the solid and evolution of speciation and interaction in the liquid with pressure.

In the Fe-Ni-S ternary system, an inflection point occurs at 5 GPa (Liu and Li, 2020) but not at 20 GPa (Gilfoy and Li, 2020) or 24 GPa (this study). These observations seem to be consistent with the appearance of intermediate Ni-S compounds at much lower pressures than their Fe-S counterparts - Ni_3S was observed at pressures as low as 5.1 GPa (Urakawa et al., 2011) and Ni_3S_2 is stable at atmospheric pressure. We speculate that at the pressures be-

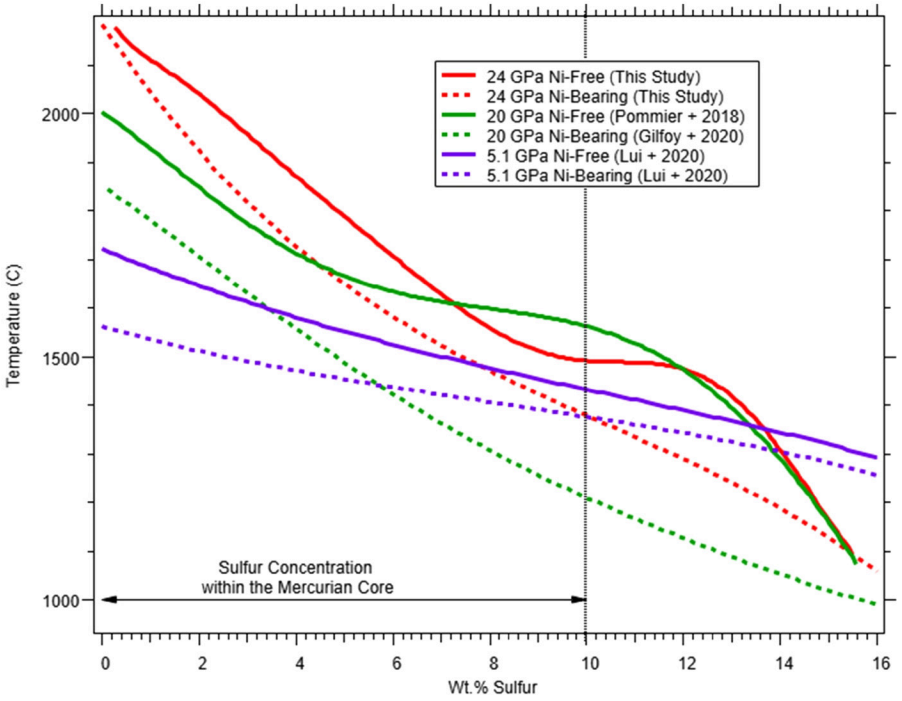

Fig. 5. Fe-S and (Fe, Ni)-S system compared to literature. At each pressure, Ni lowers the melting point of the Fe-S liquidus. The Fe-S liquidi are solid curves, and the (Fe, Ni)-S liquidi are dashed curves. Red are results from this study, where the 11-14 wt.% liquidus is used. Green is the published liquidi at 20 GPa (Pommier et al., 2018; Gilfoy and Li, 2020). Purple is published liquidi at 5 GPa (Liu and Li, 2020).

tween adjacent intermediate sulfides, the stability of a single liquid may be enhanced by the presence of multiple Fe-S species, which leads to larger entropies and hence lower Gibbs free energies. In contrast, at the pressures near the appearance of intermediate sulfides, the liquid may be dominated by one metal and one sulfide species with strong repulsion between them.

As an alloying element, Ni has relatively small effects on the density and melting point of Fe, but it may influence the physical and chemical properties of Fe significantly. Nickel is extensively used to produce stainless steel. Notably, Invar is an Fe-Ni alloy with 36% Ni that exhibits extremely low coefficient of thermal expansion, with important industrial applications. The origin of the Invar behavior remains a subject of research, and has been attributed to a disordered non-collinear configuration between the ferromagnetic and paramagnetic states at 1 bar (van Schilfgaarde et al., 1999). Further studies are needed to elucidate the underlying cause of the effects of Ni on the melting behavior of the Fe-S system as reported here and in previous studies (Gilfoy and Li, 2020; Liu and Li, 2020).

4.2. Core solidification models

The concentration of Ni between studies is highly variable; however, if we assume the effect of Ni between 7 to 40 GPa is uniform, we can calculate a pressure-temperature phase diagram (Fig. 6) of the (Fe, Ni)-S system to infer potential solidification regimes of the Mercurian core. Solidification regimes are inferred based on the intersection of the Mercurian adiabat with the (Fe, Ni)-S liquidus. We apply two different adiabats; the adiabats have a slope of 11 °C/GPa. The adiabats represent a core-mantle boundary temperature of 1427 and 1627 °C. The slope of 11 °C/GPa was calculated by Chen et al. (2008) shown in Fig. 6.

Each of the published (Fe, Ni)-S liquidi are proposed to be ideal (Stewart et al., 2007; Gilfoy and Li, 2020; Liu and Li, 2020), resulting in a gradual increase in melting point with pressure. The eutectic shift between 5 and 20 GPa results in a lower melting point at 20 GPa than 5 GPa for high-sulfur concentrations. This

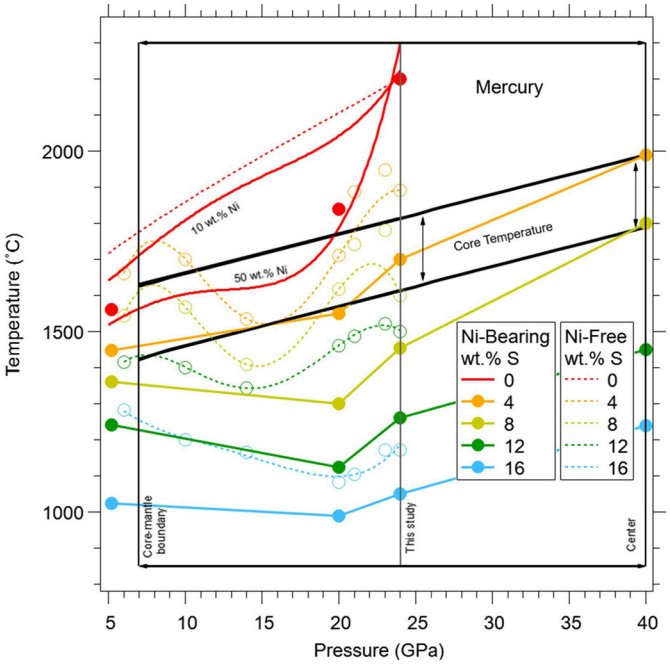

Fig. 6. Pressure-temperature phase diagram for the Mercurian core. The adiabat, core temperature, is from Chen et al. (2008) and is represented by two black lines; the black lines represent a cold and warm core and bracket a range in proposed core temperatures (vertical arrows). Ni-Free (Fe-S) liquidi are fifth-order polynomial fits to published data (open circles) at variable S concentrations (Fei et al., 2000; Stewart et al., 2007; Chen et al., 2008; Buono and Walker, 2011; Pommier et al., 2018). Ni-bearing ((Fe, Ni)-S) liquidi are linear fits between published data (closed circles) at variable S concentrations. Please note, based on available data, the Ni concentration ranges from 50 wt.%, 9 wt.%, to 11-14 wt.% at 5, 20, and 24 GPa, respectively (Gilfoy and Li, 2020; Liu and Li, 2020). The melting point of Fe-Ni is reported at 10 and 50 wt.% Ni, calculated based on 2 to -7 °C/wt.% Ni at high to low pressure, respectively (Boccato et al., 2017; Gilfoy and Li, 2020; Liu and Li, 2020).

gradual decrease in temperature results in different solidification regimes. We propose two solidification regimes for the core of

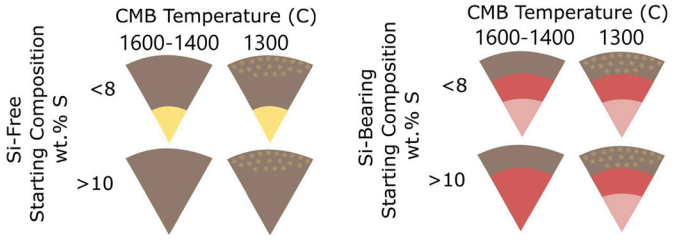

Fig. 7. Proposed solidification regimes for the Mercurian core for a range of S concentrations. They are divided into two regions left-Si free and right Si-bearing. Brown represents a molten iron-nickel-sulfur alloy, yellow represents a pure iron-nickel, red represents liquid (Fe, Ni)-Si-S, and pink represents solid (Fe, Ni)-Si. The top row represents an initial core composition with <8 wt.% S. As Mercury cools, a Fe alloy forms at the inner core; the bulk molten core composition becomes sulfur-rich, iron-nickel precipitates at the core-mantle boundary. The bottom row represents an initial composition with >10 wt.% S. Iron-nickel precipitates at the core-mantle boundary.

Mercury, shown in Fig. 7 (left). The first regime occurs when the bulk composition is <8 wt.% S, at this condition, Fe-Ni solidifies at 40 GPa; as the S concentration increases, Fe-Ni solidifies at the core-mantle boundary (7 GPa). The second solidification regime occurs when the bulk composition is >10 wt.% S and Fe-Ni solidifies at 7 GPa.

Considering the temperature profile of the Mercurian core, 11 °C/GPa with a core-mantle boundary temperature of 1400-1600 °C and a S concentration range of 0-17 wt.%, a composition of <8 wt.% S is the only compositional range that would result in a detectable partially molten core. Previous studies predict the core is partially molten via the precipitation of Fe-snow or the formation of a Fe-S shell at the core-mantle boundary (Chen et al., 2008; Malavergne et al., 2010). Suppose we assume similar solidification models for the addition of Ni. In that case, there are three possible explanations:

(i) A low core-mantle boundary temperature. For Fe-Ni snow to occur at the core-mantle boundary, the temperature must be 1300 °C or lower. This is less than the predicted range of the core-mantle boundary, 1400-1600 °C.
(ii) There is a (Fe, Ni)-S layer at the top of the Mercurian core. To form a (Fe, Ni)-S shell, we assume a core composed of (Fe, Ni)-Si-S where Si is immiscible in (Fe, Ni)-S at low pressures. This is analogous to the Fe-Si-S system, but future studies are needed to confirm the immiscibility of the (Fe, Ni)-Si-S system. The liquid (Fe, Ni)-S shell would form at >1300 °C.
(iii) A combination of i and ii. At 1300 °C, Fe-Ni snow will form at the core-mantle boundary within the (Fe, Ni)-S shell, as shown in Fig. 7 (right).

Mercury is predicted to have a magnetic field insulated by Fe snow and/or the formation of a sulfide shell. The liquidi impose constraints on the current S range and adiabat location. The most applicable solidification regime is the formation of Fe-Ni precipitation at the core-mantle boundary and 40 GPa. The formation of iron-nickel snow can explain the decrease in magnetic field strength. However, it does not occur until the core-mantle boundary is about 1300 °C. This temperature is outside the predicted core-mantle boundary range of 1400 - 1600 °C. The lower boundary of 1400 °C was based on experimental constraints on the solidification of Fe-S (Boehler, 1992; Chen et al., 2008). If Fe-Ni snow is predicted to occur at the core-mantle boundary, we propose that the core-mantle boundary temperature needs to be lowered by at least 100 °C. If a solid (Fe, Ni)S shell is predicted to occur at the core mantle boundary the core-mantle boundary temperature would need to be lowered more than 100 °C.

5. Conclusions

Experiments on the Fe-S binary system at 14 GPa confirmed the presence of an inflection point at ~10 wt.% S on the Fe-rich side of the eutectic. Experimental data at 24 GPa show that on the iron-rich side of the eutectic, the Fe-S liquidus curve has an inflection point at ~11.5 wt.% S, whereas the (Fe, Ni)-S liquidus curve does not. The presence of Ni lowers the melting point of the Fe-S system by as much as 300 °C. The effect of Ni appears to have a complex dependence on pressure and composition. Further studies are needed to quantify the impact and explore the implications for the Mercurian core's thermal and chemical state and the origin of its weak magnetic field.

CRediT authorship contribution statement

Allison Pease: Conceptualization, Data curation, Formal analysis, Funding acquisition, Investigation, Methodology, Validation, Visualization, Writing – original draft, Writing – review & editing. **Jie Li:** Conceptualization, Data curation, Funding acquisition, Investigation, Methodology, Project administration, Resources, Software, Supervision, Validation, Visualization, Writing – review & editing.

Declaration of competing interest

The authors declare that they have no known competing financial interests or personal relationships that could have appeared to influence the work reported in this paper.

Data availability

Data will be made available on request.

Acknowledgements

This work was completed at the University of Michigan. This work was supported by NASA Grant # NNX15AG54G, NSF Grant # EAR1763189, and GSA Ian S.E. Carmichael Research Award. We are grateful for the assistance provided by Owen Neill while using the SEM/EDS and EPMA. In addition, we are grateful for the assistance of undergraduate students (Will O'Neal and Brad Heint) with the preparation of experiments M113016 and M021217.

Appendix A. Supplementary material

Supplementary material related to this article can be found online at https://doi.org/10.1016/j.epsl.2022.117865.

References

Anderson, J.D., Jurgens, R.F., Lau, E.L., Slade, M.A., Schubert, G., 1996. Shape and orientation of Mercury from radar ranging data. Icarus 124, 690–697. https://doi.org/10.1006/icar.1996.0242.
Anzellini, S., Dewaele, A., Mezouar, M., Loubeyre, P., Morard, G., 2013. Melting of iron at Earth's inner core boundary based on fast. Science 340, 464–466.
Boccato, S., Torchio, R., Kantor, I., Morard, G., Anzellini, S., Giampaoli, R., Briggs, R., Smareglia, A., Irifune, T., Pascarelli, S., 2017. The melting curve of nickel up to 100 GPa explored by XAS. J. Geophys. Res., Solid Earth 122, 9921–9930. https://doi.org/10.1002/2017JB014807.
Boehler, R., 1992. Melting of the FeFeO and the FeFeS systems at high pressure: constraints on core temperatures. Earth Planet. Sci. Lett. 111, 217–227. https://doi.org/10.1016/0012-821X(92)90180-4.
Buono, A.S., Walker, D., 2011. The Fe-rich liquidus in the Fe-FeS system from 1 bar to 10 GPa. Geochim. Cosmochim. Acta 75, 2072–2087. https://doi.org/10.1016/j.gca.2011.01.030.
Chen, B., Li, J., Hauck, S.A., 2008. Non-ideal liquidus curve in the Fe-S system and Mercury's snowing core. Geophys. Res. Lett. 35, 10–14. https://doi.org/10.1029/2008GL033311.

Deng, L., Seagle, C., Fei, Y., Shahar, A., 2013. High pressure and temperature electrical resistivity of iron and implications for planetary cores. Geophys. Res. Lett. 40, 33–37. https://doi.org/10.1029/2012GL054347.

Dumberry, M., Rivoldini, A., 2015. Mercury's inner core size and core-crystallization regime. Icarus 248, 254–268. https://doi.org/10.1016/j.icarus.2014.10.038.

Fei, Y., Bertka, C.M., Finger, L.W., 1997. High-pressure iron-sulfur compound, Fe3S2, and melting relations in the Fe-FeS system. Science (New York, N.Y.) 275, 1621–1623. https://doi.org/10.1126/science.275.5306.1621.

Fei, Y., Li, J., Bertka, C.M., Prewitt, C.T., 2000. Structure type and bulk modulus of Fe3S, a new iron-sulfur compound. Am. Mineral. 85, 1830–1833. https://doi.org/10.2138/am-2000-11-1229.

Fei, Y., Li, J., Hirose, K., Minarik, W., Van Orman, J., Sanloup, C., van Westrenen, W., Komabayashi, T., Funakoshi, K., 2004. A critical evaluation of pressure scales at high temperatures by in situ X-ray diffraction measurements. Phys. Earth Planet. Inter. 143–144, 515–526. https://doi.org/10.1016/j.pepi.2003.09.018.

Gessmann, C.K., Wood, B.J., Rubie, D.C., Kilburn, M.R., 2001. Solubility of silicon in liquid metal at high pressure: implications for the composition of the Earth's core. Earth Planet. Sci. Lett. 184, 367–376. https://doi.org/10.1016/S0012-821X(00)00325-3.

Gilfoy, F., Li, J., 2020. Thermal state and solidification regime of the martian core: Insights from the melting behavior of FeNi-S at 20 GPa. Earth Planet. Sci. Lett. 541, 116285. https://doi.org/10.1016/j.epsl.2020.116285.

Harder, H., Schubert, G., 2001. Sulfur in Mercury's core? Icarus 151, 118–122. https://doi.org/10.1006/icar.2001.6586.

Hauck II, S.A., et al., 2013. The curious case of Mercury's internal structure. J. Geophys. Res., Planets 118, 1204–1220. https://doi.org/10.1002/jgre.20091.

Knibbe, J.S., van Westrenen, W., 2018. The thermal evolution of Mercury's Fe–Si core. Earth Planet. Sci. Lett. 482, 147–159. https://doi.org/10.1016/j.epsl.2017.11.006.

Leinenweber, K.D., Tyburczy, J.A., Sharp, T.G., Soignard, E., Diedrich, T., Petuskey, W.B., Wang, Y., Mosenfelder, J.L., 2012. Cell assemblies for reproducible multi-anvil experiments (the COMPRES assemblies). Am. Mineral. 97, 353–368. https://doi.org/10.2138/am.2012.3844.

Li, J., Agee, C.B., 2001. The effect of pressure, temperature, oxygen fugacity and composition on partitioning of nickel and cobalt between liquid Fe-Ni-S alloy and liquid silicate: implications for the Earth's core formation. Geochim. Cosmochim. Acta 65, 1821–1832. https://doi.org/10.1016/S0016-7037(00)00613-X.

Liu, J., Li, J., 2020. Solidification of lunar core from melting experiments on the Fe–Ni–S system. Earth Planet. Sci. Lett. 530, 115834. https://doi.org/10.1016/j.epsl.2019.115834.

Malavergne, V., et al., 2014. How Mercury can be the most reduced terrestrial planet and still store iron in its mantle. Earth Planet. Sci. Lett. 394, 186–197. https://doi.org/10.1016/j.epsl.2014.03.028.

Malavergne, V., Siebert, J., Guyot, F., Gautron, L., Combes, R., Hammouda, T., Borensztajn, S., Frost, D., Martinez, I., 2004. Si in the core? New high-pressure and high-temperature experimental data. Geochim. Cosmochim. Acta 68, 4201–4211. https://doi.org/10.1016/j.gca.2004.04.013.

Malavergne, V., Toplis, M.J., Berthet, S., Jones, J., 2010. Highly reducing conditions during core formation on Mercury: implications for internal structure and the origin of a magnetic field. Icarus 206, 199–209. https://doi.org/10.1016/j.icarus.2009.09.001.

Manthilake, G., Chantel, J., Monteux, J., Andrault, D., Bouhifd, M.A., Bolfan Casanova, N., Boulard, E., Guignot, N., King, A., Itie, J.P., 2019. Thermal conductivity of FeS and its implications for Mercury's long-sustaining magnetic field. J. Geophys. Res., Planets 124, 2359–2368. https://doi.org/10.1029/2019JE005979.

Margot, J.L., Peale, S.J., Jurgens, R.F., Slade, M.A., Holin, I.V., 2007. Large longitude libration of Mercury reveals a Molten core. Science 316, 710–714. https://doi.org/10.1126/science.1140514.

McCubbin, F.M., Riner, M.A., Vander Kaaden, K.E., Burkemper, L.K., 2012. Is Mercury a volatile-rich planet? Geophys. Res. Lett. 39. https://doi.org/10.1029/2012GL051711.

Michel, N.C., Hauck II, S.A., Solomon, S.C., Phillips, R.J., Roberts, J.H., Zuber, M.T., 2013. Thermal evolution of Mercury as constrained by MESSENGER observations. J. Geophys. Res., Planets 118, 1033–1044. https://doi.org/10.1002/jgre.20049.

Morard, G., Andrault, D., Guignot, N., Siebert, J., Garbarino, G., Antonangeli, D., 2011. Melting of Fe–Ni–Si and Fe–Ni–S alloys at megabar pressures: implications for the core–mantle boundary temperature. Phys. Chem. Miner. 38, 767–776. https://doi.org/10.1007/s00269-011-0449-9.

Namur, O., Charlier, B., Holtz, F., Cartier, C., McCammon, C., 2016. Sulfur solubility in reduced mafic silicate melts: implications for the speciation and distribution of sulfur on Mercury. Earth Planet. Sci. Lett. 448, 102–114. https://doi.org/10.1016/j.epsl.2016.05.024.

Ness, N.F., Behannon, K.W., Lepping, R.P., Whang, Y.C., 1976. Observations of Mercury's magnetic field. Icarus 28, 479–488. https://doi.org/10.1016/0019-1035(76)90121-4.

Nittler, L.R., Chabot, N.L., Grove, T.L., Peplowski, P.N., 2018. The chemical composition of Mercury. In: Solomon, S.C., Nittler, L.R., Anderson, B.J.E. (Eds.), Mercury: The View After MESSENGER. In: Cambridge Planetary Science. Cambridge University Press, pp. 30–51.

Pommier, A., 2020. Experimental investigation of the effect of nickel on the electrical resistivity of Fe-Ni and Fe-Ni-S alloys under pressure. Am. Mineral. 105, 1069–1077. https://doi.org/10.2138/am-2020-7301.

Pommier, A., Laurenz, V., Davies, C.J., Frost, D.J., 2018. Melting phase relations in the Fe-S and Fe-S-O systems at core conditions in small terrestrial bodies. Icarus 306, 150–162. https://doi.org/10.1016/j.icarus.2018.01.021.

Pommier, A., Leinenweber, K., Tran, T., 2019. Mercury's thermal evolution controlled by an insulating liquid outermost core? Earth Planet. Sci. Lett. 517, 125–134. https://doi.org/10.1016/j.epsl.2019.04.022.

Riner, M.A., Bina, C.R., Robinson, M.S., Desch, S.J., 2008. Internal structure of Mercury: implications of a Molten core. J. Geophys. Res., Planets 113. https://doi.org/10.1029/2007JE002993.

Saunders, N., Miodownik, A.P., Miodownik, A.P., 1998. CALPHAD (Calculation of Phase Diagrams): a Comprehensive Guide. Elsevier Science & Technology, London, United Kingdom. http://ebookcentral.proquest.com/lib/michstate-ebooks/detail.action?docID=318294.

Shen, G., Mao, H., Hemley, R.J., Duffy, T.S., Rivers, M.L., 1998. Melting and crystal structure of iron at high pressures and temperatures. Geophys. Res. Lett. 25, 373–376. https://doi.org/10.1029/97GL03776.

Stevenson, D.J., Spohn, T., Schubert, G., 1983. Magnetism and thermal evolution of the terrestrial planets. Icarus 54, 466–489. https://doi.org/10.1016/0019-1035(83)90241-5.

Stewart, A.J., Schmidt, M.W., van Westrenen, W., Liebske, C., 2007. Mars: a new core-crystallization regime. Science 316, 1323–1325. https://doi.org/10.1126/science.1140549.

Tao, R., Fei, Y., 2021. High-pressure experimental constraints of partitioning behavior of Si and S at the Mercury's inner core boundary. Earth Planet. Sci. Lett. 562, 116849. https://doi.org/10.1016/j.epsl.2021.116849.

Tosi, N., Grott, M., Plesa, A.-C., Breuer, D., 2013. Thermochemical evolution of Mercury's interior. J. Geophys. Res., Planets 118, 2474–2487. https://doi.org/10.1002/jgre.20168.

Urakawa, S., Matsubara, R., Katsura, T., Watanabe, T., Kikegawa, T., 2011. Stability and bulk modulus of Ni3S, a new nickel sulfur compound, and the melting relations of the system Ni-NiS up to 10 GPa. Am. Mineral. 96, 558–565. https://doi.org/10.2138/am.2011.3578.

van Schilfgaarde, M., Abrikosov, I.A., Johansson, B., 1999. Origin of the Invar effect in iron-nickel alloys. Nature 400, 46–49. https://doi.org/10.1038/21848.

Vilim, R., Stanley, S., Hauck II, S.A., 2010. Iron snow zones as a mechanism for generating Mercury's weak observed magnetic field. J. Geophys. Res., Planets 115. https://doi.org/10.1029/2009JE003528.

Williams, Q., Jeanloz, R., 1990. Melting relations in the iron-sulfur system at ultra-high pressures: implications for the thermal state of the Earth. J. Geophys. Res., Solid Earth 95, 19299–19310. https://doi.org/10.1029/JB095iB12p19299.

Zhang, L., Fei, Y., 2008. Effect of Ni on Fe – FeS phase relations at high pressure and high temperature. Earth Planet. Sci. Lett. 268, 212–218. https://doi.org/10.1016/j.epsl.2008.01.028.

Zhang, D., Jackson, J.M., Zhao, J., Sturhahn, W., Alp, E.E., Hu, M.Y., Toellner, T.S., Murphy, C.A., Prakapenka, V.B., 2016. Temperature of Earth's core constrained from melting of Fe and Fe0.9Ni0.1 at high pressures. Earth Planet. Sci. Lett. 447, 72–83. https://doi.org/10.1016/j.epsl.2016.04.026.

Zolotov, M.Y., Sprague, A.L., Hauck II, S.A., Nittler, L.R., Solomon, S.C., Weider, S.Z., 2013. The redox state, FeO content, and origin of sulfur-rich magmas on Mercury. J. Geophys. Res., Planets 118, 138–146. https://doi.org/10.1029/2012JE004274.

Zurbuchen, T.H., Raines, J.M., Gloeckler, G., Krimigis, S.M., Slavin, J.A., Koehn, P.L., Killen, R.M., Sprague, A.L., McNutt, R.L., Solomon, S.C., 2008. MESSENGER observations of the composition of Mercury's ionized exosphere and plasma environment. Science 321, 90–92. https://doi.org/10.1126/science.1159314.